PHYSICAL REVIEW E **70**, 036605 (2004)

Optical properties of an ideal homogeneous causal left-handed material slab

P. F. Loschialpo, D. W. Forester, D. L. Smith, and F. J. Rachford
Naval Research Laboratory, Washington, D.C. 20375, USA

C. Monzon
SFA/NRL, Largo, Maryland 20774, USA

(Received 1 August 2003; revised manuscript received 3 June 2004; published 16 September 2004)

The optical properties of a homogeneous slab of material characterized by causal permittivity $\varepsilon(f)$, and permeability $\mu(f)$ are investigated through finite difference time domain simulations. Lorentzian $\varepsilon(f)$ and $\mu(f)$ are used to produce values of interest in the resulting index $n(f)$, namely, $n<0$, $0<n<1$, and $n\approx 0$. Negative refraction of both cw and pulsed waves is observed when operated in the left-handed medium (LHM) regime. In particular, we examined materials having both an impedance matched to free space and an impedance not matched to free space, as is the case of a split-ring resonator structure, and find it to exhibit LHM behavior, in agreement with previously published claims. Spherical aberration and channeling are observed as the magnitude of the negative index is increased beyond -1. Critical angle phenomena are seen for indices in the range $0<n<1$, and a spatial filter effect is identified in the $n\approx 0$ region. A transmission bandpass in the vicinity of $n\approx 0$ is identified as a "ferromagnetic antiresonance," where the material acts as both a frequency and a spatial filter.

DOI: 10.1103/PhysRevE.70.036605 PACS number(s): 41.20.Jb, 42.70.Qs, 78.20.Ci, 77.22.Ch

I. INTRODUCTION

About 40 years ago Veselago [1] proposed a hypothetical negative index material that he named a "left-handed medium" (LHM), which was characterized by a rather unusual property, namely, that the phase velocity and energy flow point in opposite directions. It was not until recently that experiments were performed to combine real materials believed to have simultaneous negative μ and ε, to test Veselago's gedanken experiment. LHMs have been the focus of intense research in recent years. Most LHM studies employ plane-parallel boundaries because the lumped elements used to produce negative μ and ε conform more readily to such geometries. Veselago used this geometry and predicted that such a planar LHM slab would produce two distinct foci, thus acting as a lens for an external point source.

The unusual properties of LHMs and the scarcity of materials available for experiments have contributed to considerable controversy over their expected optical properties, in particular for LHM slabs. For example, Valanju *et al.* [2] relate that some researchers [3–9] have erroneously concluded that a plane-parallel slab of a LHM can focus an electromagnetic pulse diverging from a point source. Garcia *et al.* [10] also questioned the interpretation of measurements by those researchers, and argued that the peaks in transmission spectra for split-ring resonator (SRR) structures were not evidence of a left-handed material, but rather evidence of a "zero permeability" material having $\mathrm{Re}(\mu)\approx 0$. Garcia and co-workers [10,11] identified deficiencies in wedge transmission experiments, which lead to ambiguities in the determination of the index of refraction for such materials. Pendry and Ramakrishna [3,4] have taken the focusing argument to another level by insisting that LHMs can amplify evanescent modes, allowing a complete reconstruction of the point source to a perfect point image, with none of the conventional optical limitations. Smith *et al.* [12] later pointed out that a perfect point image can be achieved only for source-to-image distances much less than one wavelength, unless the losses are exceedingly small.

An experimental LHM structure is a composite material where the electric and magnetic properties are emulated through periodic arrays of discrete elements. In the case of SRR structures, the elements are smaller than the wavelength of illumination [6–9,13]. In other experiments, photonic band gap structures composed of metallic disks have been used [14]. All of these structures have physical limitations that present problems in any effort to characterize the intrinsic effective indices of refraction for them. In particular, the structures are inhomogeneous, anisotropic, lossy, and not impedance matched to the surrounding medium.

In light of the continuing dialogue on these topics [2–19] we have elected to perform accurate and thorough numerical simulations for hypothetical LHM slabs having causal frequency-dependent intrinsic properties. Our study is broken into sections, the initial part being directed at slabs that are impedance matched to free space to reduce the complication of front face reflection. We examine the optical properties over the frequency range where the index of refraction has the values $n<0$, to $0<n<1$, and $n\approx 0$. The optical properties in each of these frequency regions are distinctly different. The case where $n<0$ has been previously reported [19,20] but is nonetheless instructive to repeat in order to demonstrate that the focus is a fundamental property of the LHM. Focusing, or alternatively channeling, is observed depending on the value of the negative index. Simulations in the range for which $0<n<1$ reveal additional optical properties not seen in ordinary materials. For example, since refracted rays are bent away from the normal, in contrast to those of an ordinary material, a critical angle is observed, beyond which there is total reflection. Unusual behavior is seen for $n \approx 0$, with possible application in the design of a highly directive antenna.

Real life materials are not impedance matched to free space [21]. While impedance mismatched LHM, having $Z \neq 1$ and $n < 0$, also exhibit the focusing or channeling properties observed for the matched material, the impedance mismatch results in reflections from the front and rear boundaries. We examine these optical effects over the same range of negative index values as for the matched material. In this latter case, we vary n by varying ε while keeping μ constant.

Similarly, we investigate the region $\mu \approx 0$, historically referred to as the ferromagnetic antiresonance [22], where a transmission peak in the spectrum is found. Garcia *et al.* [10] refer to a material exhibiting this property as a "zero permeability material" and attribute the observations in SRR spectral data by other researchers to this phenomenon. We find that this peak appears only in materials having a significant nonzero imaginary component to the permittivity. We discuss the advantages that slab measurements may have over wedge measurements in distinguishing between the different refractive regions $n < 0$, $0 < n$, and $n \approx 0$.

Finally we examine the SRR structure reported by Smith *et al.* [7] in order to shed some light on the controversy surrounding the interpretation of the transmission spectra for SRR structures. Specifically, we find that the transmission band in [7] is in a LHM region where $n < 0$ and focusing is observed. We also find evidence of focusing by a planar slab having these dielectric properties. Care must be exercised in interpreting transmission data from composite LHM structures. The transmission data must be analyzed together with measured or computed field distributions in planar slab geometry. For a determination of the refractive properties of a material, the slab geometry is preferred over a wedge. As Garcia *et al.* pointed out, energy is transmitted preferentially in the thinner portion of the wedge, which can cause the measured far-field distribution to be misinterpreted as negative refraction.

II. ANALYSIS

As the index is a dominant feature for refraction and propagation, our study is organized according to the index. Through extensive simulations we unveil all the different regimes of operation of generic materials, namely, $n < 0$, $0 < n < 1$, and $n \approx 0$. We exclude ordinary materials $(n > 1)$ from our presentation, and we employ a Gaussian modulated carrier excitation in order to elucidate the negative refraction of pulsed waves. For convenience we split this section into two parts, one dealing with impedance matched materials and another which includes more realistic materials that are not impedance matched.

Negative index properties are encountered when both $\varepsilon(f)$ and $\mu(f)$, the intrinsic permittivity and permeability, respectively, are strongly dispersive and simultaneously negative over a limited frequency range. An important requirement to be imposed on a medium of any type is that its constitutive parameters be causal. The Debye and Drude models have been employed previously in connection with LHMs. In the present study we have adopted for our hypothetical materials (which include the SRR model), a Lorentzian frequency dependence for both ε and μ of the form

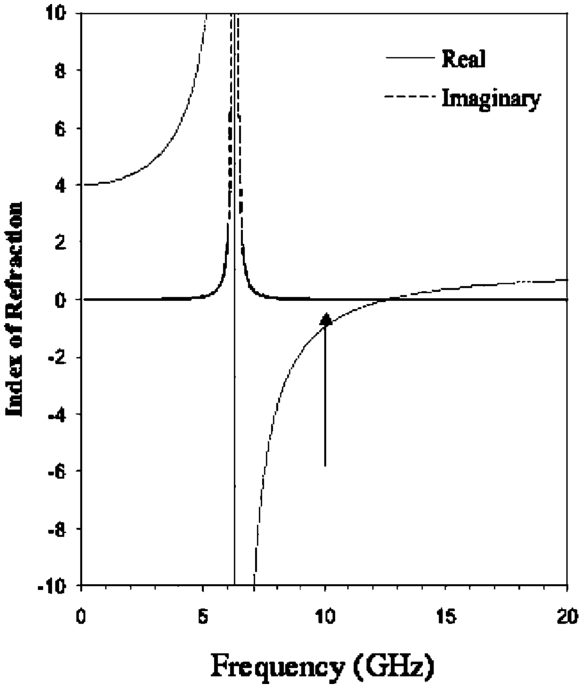

FIG. 1. Index of refraction corresponding to $\varepsilon(f) = \mu(f)$ which assume the functional form of Eq. (1) for $G = 0.04$ GHz, $\varepsilon_{DC} = \mu_{DC} = 4.0$, and $f_0 = 6.3$ GHz. The arrow points to the 10 GHz operating point where the index $n(f) \approx -1$.

$$F(f) = 1 + \frac{K-1}{1 - i(fG/f_0^2) - (f/f_0)^2}. \tag{1}$$

We take $F(f) = \mu(f)$ or $\varepsilon(f)$ and $K = \mu_{DC}$ or ε_{DC}.

A. Medium impedance matched to free space

We first consider materials for which $\varepsilon(f) = \mu(f)$. The resulting medium does possess a complex index of refraction $n(f)$, which acquires positive, negative, or zero values as the frequency is varied, and hence allows us to investigate the physics of propagation without loss of generality. The complex index of refraction is given by $n(f) = \sqrt{\varepsilon(f)}\sqrt{\mu(f)}$. Considering the effect of low losses via $G = 0.04$ GHz, $\varepsilon_{DC} = \mu_{DC} = 4.0$, and $f_0 = 6.3$ GHz, the functional form of the index is plotted in Fig. 1. In particular, at 10 GHz, the index assumes the value $n(f) \approx -1.001 + i0.013 \approx -1$, indicating that the losses are quite low.

Our simulations were carried out with a finite difference time domain (FDTD) code [23] that models $\varepsilon(f)$ and $\mu(f)$ using causal frequency dependences and has been validated extensively by comparisons with laboratory experiments. Our models employ perfectly-matched-layer [24] absorbing boundaries in the dimensions of finite extent and periodic boundary conditions in the dimension of infinite extent. The simulations were performed on a two-dimensional geometry, which, while retaining generality, reduces computational time significantly. For the majority of runs in our study, the

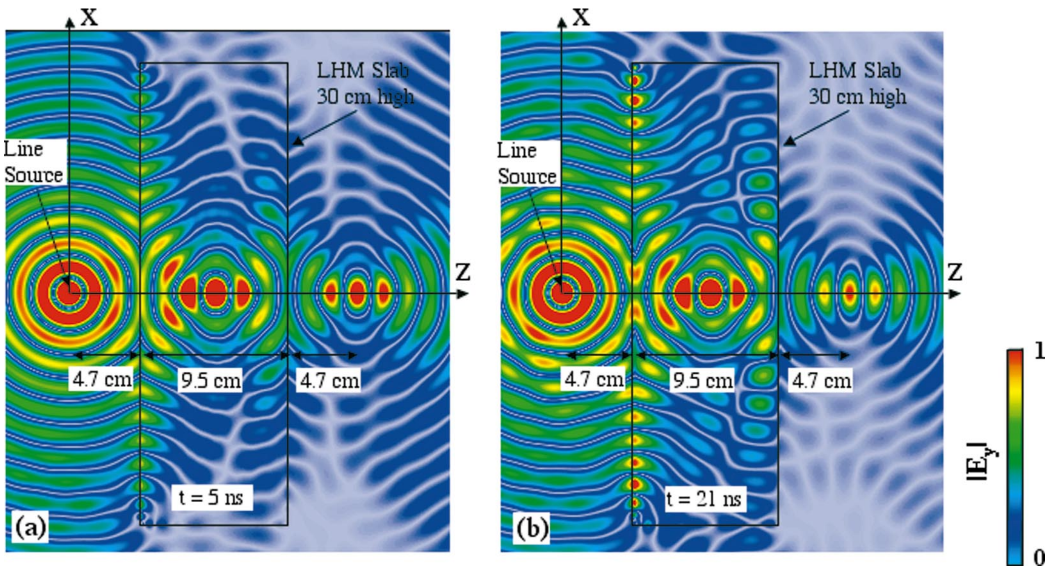

FIG. 2. (Color) FDTD snapshots of the electric field magnitude at $t=$ (a) 5 ns and (b) 21 ns for a planar slab with line source illumination at 10 GHz (LHM regime). The position of both focal points is in agreement with Snell's law. The stability of the foci images is established by comparison of (a) with (b). The rectangle shown in the figures represents the slab contour. The height of the slab is $10\lambda_0$.

volume of our two-dimensional FDTD simulation space was 700×600 cells. Each spatial cell was 0.05 cm on a side and the time step interval was $\Delta t=\Delta z\sqrt{3}c=1$ ps to satisfy the Courant condition. The illumination is provided by an electric line source oriented along the y axis.

1. Left-handed material regime $(n\approx-1)$

Our first FDTD simulation demonstrates that waves propagating from a divergent source are negatively refracted at the interface between air and LHM slabs. After a time-harmonic steady state is attained, two stable and well-defined foci are observed, as predicted by Veselago.

A line source with a 10 GHz cw is used to produce a cylindrical (divergent) wave which illuminates the LHM slab beginning at time t=0. The planar slab is at a distance $H=1.6\lambda_0$ away from the line source (see Fig. 2), and has a thickness $2H$ in the z direction and an extent $L=10.0\lambda_0$ in the x direction (free space $\lambda_0=3.0$ cm). Following initiation of the electromagnetic wave, it takes approximately 5 ns for a steady state to develop within the spatial extent of our $10.0\lambda_0$ simulation space. Subsequent analysis of the time-evolving electric field distribution reveals that the divergent line source is imaged both in the center of the slab and at a distance H behind it. The size of both foci is comparable to λ_0, as predicted by diffraction-limited optics. Figures 2(a) and 2(b) show snapshots of the electric field magnitude at $t=5$ ns and 21 ns and serve to illustrate this point. The positions of both foci are in agreement with Snell's law. Stability of the images of the foci is established by comparison of Fig. 2(a) with Fig. 2(b).

The clearly defined focal points are consistent with recent work by Ziolkowski [20] who performed FDTD calculations on an $n=-1$, impedance matched, LHM slab using a Drude model for the index. We note that the focus is not stable until the harmonic steady state is reached. The focal points appear to be distorted primarily by aberration effects including material losses, compounded by the finite extent of the material model. Time animations illustrate that the phase fronts do progress backward inside the LHM slab. This is in contrast with the forward moving phase fronts outside the slab. Guided surface waves or polaritons [25,26] are visible on the front surface of the slab in Fig. 2. In this simulation the distance of the polaritons from the images is greater than λ_0 in distance. Unlike observations reported by Chen *et al.* [26], we observe no serious degradation of image quality, which is not surprising in light of the large distance from the slab surface to the image. Our slab thickness is much larger than that considered by Chen *et al.* because we are interested in image formation beyond the near field. Chen *et al.*'s analysis also neglected losses (which may attenuate the amplitude of the polaritons).

In order to address the question as to whether the focal point is significantly affected by edge diffraction or other imperfections of the numerical model, we doubled the height of the slab, L, from $10\lambda_0$ to $20\lambda_0$, thereby reducing the influence of edge diffraction. The geometry is otherwise unaltered. Figure 3 shows a snapshot at $t=21$ ns, where once again two clear focused images are evident. Closer examination of the images reveals that the size and location of the focal points did not change as L was doubled. We conclude that edge diffraction, while apparent near the corners of the slab, does not significantly affect the characteristics of the focused images.

If the operation were diffraction limited, the size of the focal points would scale directly with λ_0. The next simulation reveals the effect of doubling the frequency of operation from 10 GHz to 20 GHz, while retaining the original slab ($9.5\text{ cm}\times30\text{ cm}$) and the same negative index (i.e., $n=-1.001+i0.013$, which requires $G=0.08$ GHz, $f_0=12.6$ GHz, $\varepsilon_{DC}=\mu_{DC}=4.0$). Figures 4(a) and 4(b) show two snapshots at 5 and 21 ns, respectively, where we observe the same focal point region. This is clear indication of the sta-

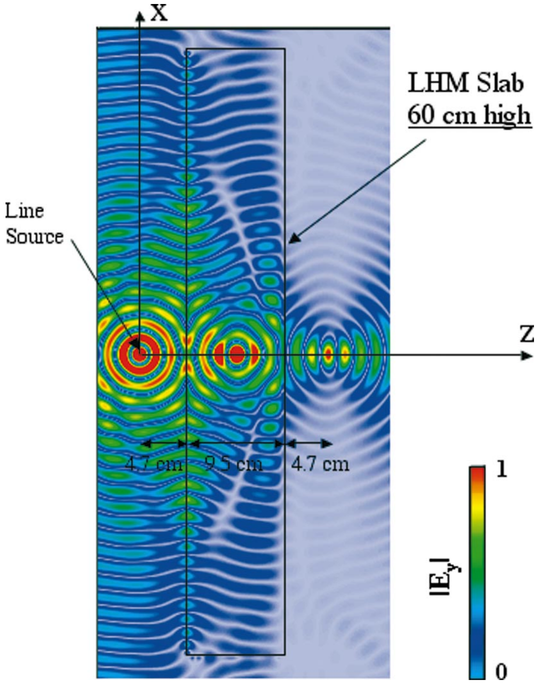

FIG. 3. (Color) FDTD snapshots for a LHM planar slab with line source illumination. The conditions are similar to those of Fig. 2(b), the only difference being the height of the slab, L, which is now doubled to $20\lambda_0$. The good agreement with Fig. 2(b) indicates that truncation effects due to the finiteness of the slab do not affect the focusing characteristics significantly.

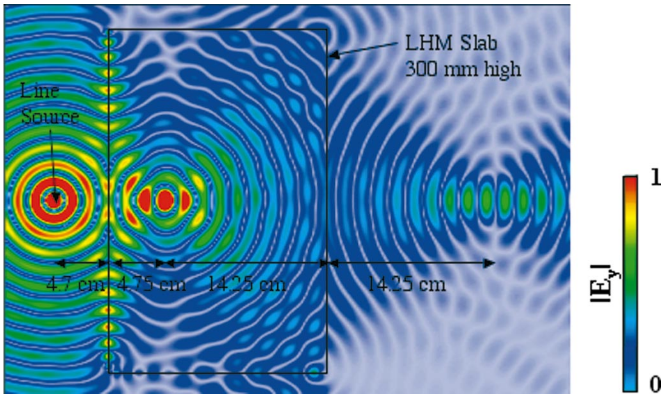

FIG. 5. (Color) Effect of doubling the slab thickness to $6.3\lambda_0$. All other conditions remain the same. The figure is a snapshot at $t = 34$ ns. The simulation demonstrates that the image plane of the LHM lens is not restricted to the near field.

bility of the solution over time, and shows that the focal size is still $\sim\lambda_0$, consistent with conventional wave optics. In view of the work of Smith *et al.* [12], it is not surprising that we see no evidence of evanescent mode amplification. The imaginary components of ε and μ would have to be much smaller, in fact, exceedingly small, for slabs having a thickness on the order of one wavelength or larger to induce subwavelength focusing.

Next we demonstrate that image formation is not a near-field effect. This is done at 10 GHz by doubling the thickness of the slab to 19 cm × 30 cm. Figure 5 displays a snapshot at 34 ns, well after the time-harmonic steady state has been established. We see that, consistent with Snell's law, the external focal point has moved out to a distance nearly $5\lambda_0$ away from the back surface, i.e., outside the near-field range of the slab. The external focus is noticeably weaker than the corresponding focal point of Fig. 2 because of the nonzero losses.

2. Left-handed material regime with variable negative index

It is informative to examine how the optical characteristics of the slab lens shown in Fig. 2 evolves as the index is

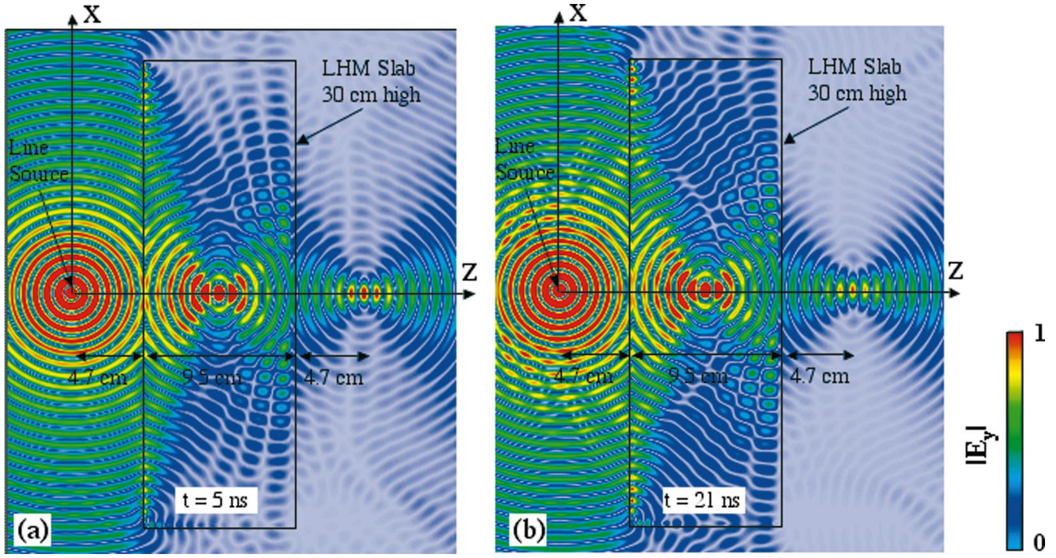

FIG. 4. (Color) FDTD snapshots at $t =$ (a) 5 ns, and (b) 21 ns, for a 30 cm high planar slab with line source illumination. Operation is at 20 Ghz (twice the earlier frequency), the region where the material is made a LHM by proper choice of parameters: $G = 0.08$ GHz, $\varepsilon_{DC} = \mu_{DC} = 4.0$, and $f_0 = 12.6$ GHz. The position of both focal points is in agreement with Snell's law. The stability of the foci images is established by comparison of (a) with (b). The rectangle shown in the figures represents the slab contour.

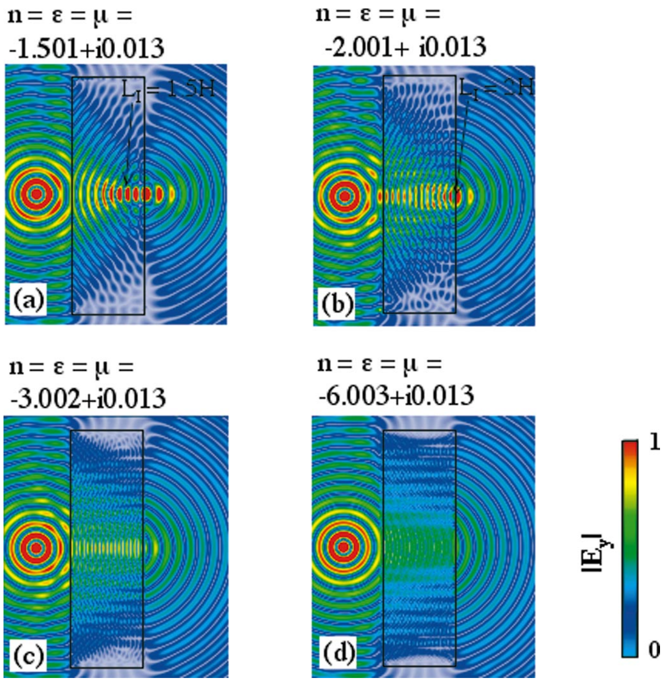

FIG. 6. (Color) FDTD snapshots for an $\varepsilon = \mu$ LHM slab as n is progressively changed from (a) $n = -1.5$ to (d) $n = -6.0$. The images become less well defined due to spherical aberration. When the distance of the first image inside the slab, L_I, is greater than the slab thickness of $2H$, there are no focused images. Channeling occurs in the extreme case where $n \ll -1$.

varied from the previous value of -1 to -6, the index value at which Ziolkowski reported a channeling effect [20]. Both ε and μ are varied simultaneously to keep the material impedance matched. Figure 6(a) shows the field magnitude for $n = -1.501 + i0.014 \approx -1.5$. The image inside the slab, computed from Snell's law, has moved away from the center, from a distance H from the front face to a distance $1.5H$ from the front face. The focus has become blurred because of an effect analogous to spherical aberration in conventional curved lenses. That is, the focal point is dependent on the angle of an incident ray whenever n deviates from -1. The image outside of the slab has moved inward to a distance $H/3$ from the rear face of the slab. As the index decreases, the image inside the slab moves outward and becomes progressively more blurred. One can see from Fig. 6(b) that the image has moved to a distance $2H$ from the front face when $n = -2.001 + i0.017 \approx -2.0$. No second images appear outside the slab since this focus is at the far edge of the slab. Further decrease in the index results in wave fronts becoming increasingly parallel to the front face inside the slab. As expected we see no images of the source in Fig. 6(c), which was computed using $n = -3.002 + i0.022 \approx -3$. Finally, when $n \ll 0$, as is the case in Fig. 6(d) where $n = -6.003 + i0.013 \approx -6$ channeling is observed inside the slab. As a result of Snell's law, all refraction is parallel to the unit normal to the interfaces, e.g., the internal field is almost a parallel beam.

3. Region with $0 < n < 1$

Negative index materials offer another interesting region where the index is positive but less than 1. From our $\varepsilon(f) = \mu(f)$ idealized material, a broad frequency interval exists where the real part of the index has a value between zero and 1. Although the material is not "left handed," unusual optical phenomena occur for this index region. Using the original parameters $G = 0.04$ GHz, $f_0 = 6.3$ GHz, and $\varepsilon_{DC} = \mu_{DC} = 4.0$ we find $n = +0.670 + i0.001$ at 20 GHz. Figure 7 is a snapshot at 21 ns, for a 20 GHz cw incident on the original slab ($9.5\ \text{cm} \times 30\ \text{cm}$). It illustrates how the wave fronts are refracted away from the normal, which is the opposite of ordinary materials. Another intriguing feature is the presence of a critical angle that occurs because the refracting material has a lower index. The critical angle is roughly $\arcsin(0.670) \approx 42°$ for this material, and any spectral ray component exceeding 42° is totally reflected, giving rise to the interference patterns to the left of the slab.

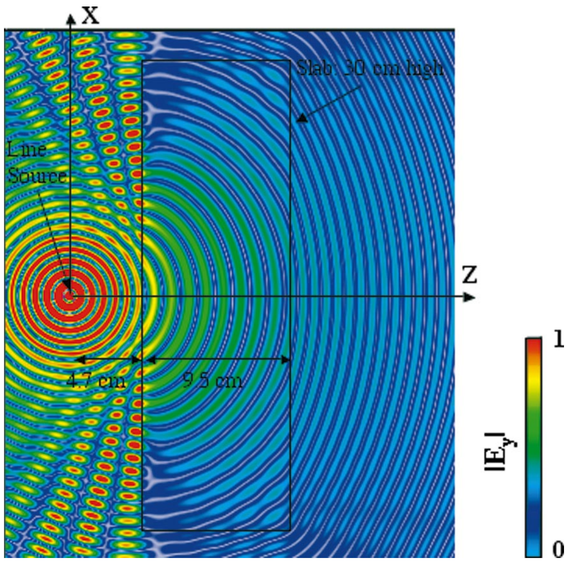

FIG. 7. (Color) FDTD snapshot of the electric field magnitude at $t = 21$ ns, for operation at 20 GHz with an index $n = +0.670 + i0.001$. The figure illustrates the refraction properties of the planar slab and exhibits critical angle phenomena.

4. Region with $n \approx 0$

In the $n \approx 0$ region, the material exhibits unique, and potentially useful, optical properties. Application of Snell's law at the air-LHM interface under the condition $n \approx 0$ translates into an explicit requirement for normally incident waves on the air side. Even though we have chosen $\varepsilon(f) = \mu(f)$ to impedance match the slab to free space, no other plane-wave component can be transmitted through the slab. Inside the slab the wavelength is nearly infinite because $\text{Re}(n) \approx 0$, indicating lack of spatial phase variation and quasistatic field oscillations over the entire area of the slab.

At 12.6 GHz our original hypothetical material has a very small index $n = 0.000 + i0.004$. Under these conditions, a cylindrical wave will react dramatically with a planar slab ($9.5\ \text{cm} \times 30\ \text{cm}$). Wave fronts incident on the slab tend to flatten out upon transmission in order to satisfy Snell's law. This phenomenon is seen in Figs. 8(a) and 8(b), which contain snapshots taken 23 ps apart (approximately 1/4 period)

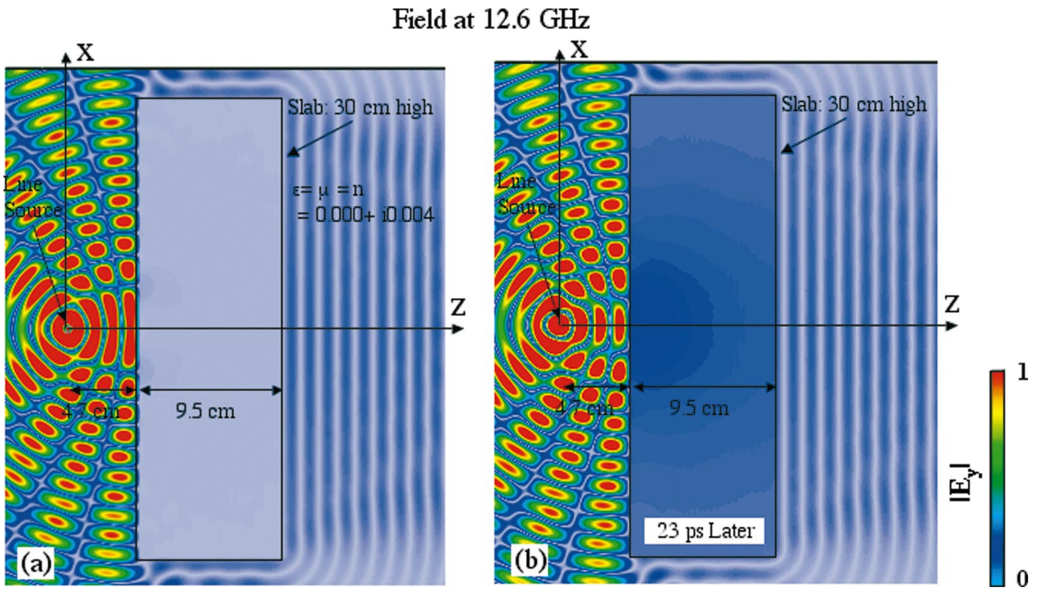

FIG. 8. (Color) Transmission through a slab with index nearly zero, $n=0$. The figures are FDTD snapshots of the electric field magnitude taken at (a) $t \approx 21$ ns and (b) another 23 ps later (approximately 1/4 period), and show distinctive flattening of wave phase fronts upon transmission. The dimensions of the slab and line source location are unchanged.

at $t \approx 21$ ns. The figures show that a single plane wave propagates from the rear side of the slab in the direction of the normal. The material is, in effect, a spatial filter. This phenomenon suggests the possibility of using planar slabs of such materials as an alternative to conventional curved lenses or reflectors for highly directive antennas. The observation is consistent with work by Enoch *et al.* [27], who proposed embedding a source inside a low-index material as a way of creating a directional antenna. It should be noted that the ratio of the transmitted electric field to the incident field (to the front of the slab) is only 0.09. This is equal to one-tenth the transmission coefficient of the slab for a normally incident plane wave.

The transmission efficiency of this spatial filter must be enhanced for practical applications. We demonstrate that reducing the slab thickness to 0.95 cm and placing a metal plate 1.2 cm ($\lambda_0/2$) behind the front face increases the transmission. The source is located midway between the metal plate and the slab front face. The simulation for this configuration is shown in Fig. 9. The transmission coefficient has tripled, going from ≈ 0.09 to ≈ 0.26. This translates to roughly a tenfold increase in power. Further improvements can be achieved with a more detailed antenna design.

5. Finite duration pulsed wave with $\mathbf{n \approx -1}$

We now examine the negative refraction of modulated finite duration pulses via a line source with a Gaussian pulse modulated 10 GHz carrier:

$$\frac{E(t')}{E_{\max}} = e^{-(t'/\tau_B)^2/2}\sin\left(\frac{2\pi t'}{\tau_P}\right). \tag{2}$$

The modulation parameter $\tau_B = 1.67$ ns, the period $\tau_P = 0.10$ ns, and the pulse peaks at 6.8 ns. A Fourier transform of Eq. (2) yields frequency components having a range of ±0.21 GHz (measured at 10% of the peak amplitude) on either side of the 10 GHz carrier. The normalized spectral amplitude is plotted in Fig. 10 as a function of the frequency. The slab is 9.5 cm × 30 cm, and the materials properties are those of Sec. A, thereby resulting in $n \approx -1$, in the frequency range of interest.

Figure 11 consists of two snapshots, (a) at $t = 6.6$ ns, as the Gaussian pulse excitation nears its peak, and (b) a snapshot

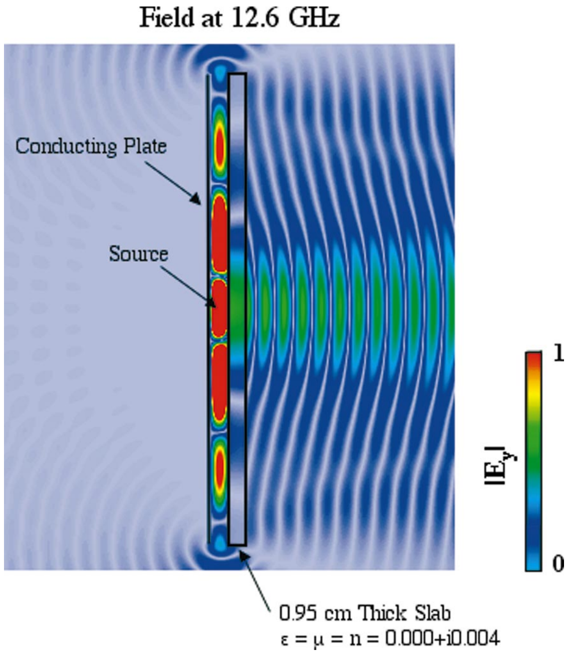

FIG. 9. (Color) An example of how a material having a nearly zero index could be used to generate pane waves with a larger amplitude. The slab thickness is reduced to 0.95 cm and a conducting plate is located $\lambda_0/2$ behind the slab. The field transmission coefficient is three times that of the configuration shown in Fig. 8.

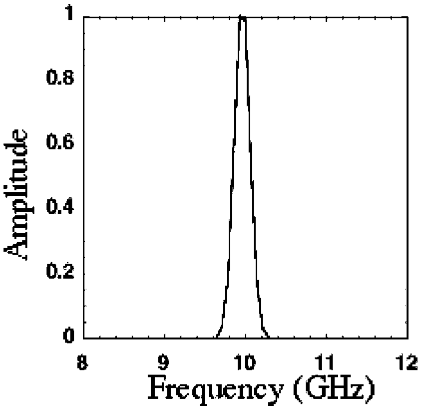

FIG. 10. Spectral components of the Gaussian pulse modulated signal Eq. (2) with $\tau_B=1.67$ ns and $\tau_P=0.10$ ns.

at $t=9.4$ ns, well after the pulse has passed. Distinct focal areas are present both at the center of the slab and equidistant to the right of the slab at both times. Although the focusing is not perfect, the size of the focal points is similar to that of Fig. 2, both of which are consistent with limitations imposed by wave optics. This comparison also indicates that chromatic aberration has a small effect on the focal regions.

Figure 12 shows the time evolution of the E_y fields on the centerline $(x=0)$ generated by the Gaussian pulse excited line source. At the source location $(z=4.7$ cm), the wave packet builds in amplitude, reaches a peak at $t\approx 7$ ns, and then decays. The figure also shows that the wave packet comes to a focus in the center of the LHM slab at a later time. Dispersion and loss have led to a reshaping and reduction of amplitude, but the wave packet maintains its overall shape. This is a clear indication that negative refraction of the pulse has occurred. The transmitted wave packet later converges to a focus in the free-space region to the right of the slab at $t\approx 9$ ns. Upon close examination we note a negative slope of the wave fronts, indicating negative phase velocity within the LHM slab.

B. Mismatched impedance materials

We examine below the optical properties of impedance mismatched LHMs over a wide range of refractive index values. We can think of these cases as either more general or more realistic models since ε is not constrained to match μ. As a particular case, and in light of comments by Garcia *et al.* [10], we also examine the SRR structure discussed in the report by Smith *et al.* [7].

1. Left-handed material regime with variable negative index

Simulations were performed for a LHM slab of refractive index between −1.5 and −6.0. The permeability was fixed at $\mu=-1.001+i0.013$, and the 10 GHz data are shown in Fig. 13. Focused images and spherical aberration effects are seen at the lower index values $n\approx-1.5$ and $n\approx-2.0$, which are similar to those of the corresponding impedance matched slab seen in Fig. 6. Likewise, channeling is again observed at large index values, such as $n\approx-6.0$. Impedance mismatches, which become progressively greater with higher index values, are manifested as large reflections from the slab surfaces. Interference patterns are especially prominent in front of the slab. The transmitted amplitudes are also smaller as compared with Fig. 6.

2. Region with $n\approx 0$: Ferromagnetic antiresonance

As mentioned by Garcia *et al.* [10], there is a transmission band in the vicinity of $\mu\approx 0$ (for normally incident plane waves), which makes this mode of operation potentially useful for implementation of narrowband frequency filters. There is also interest in this mode of operation because of

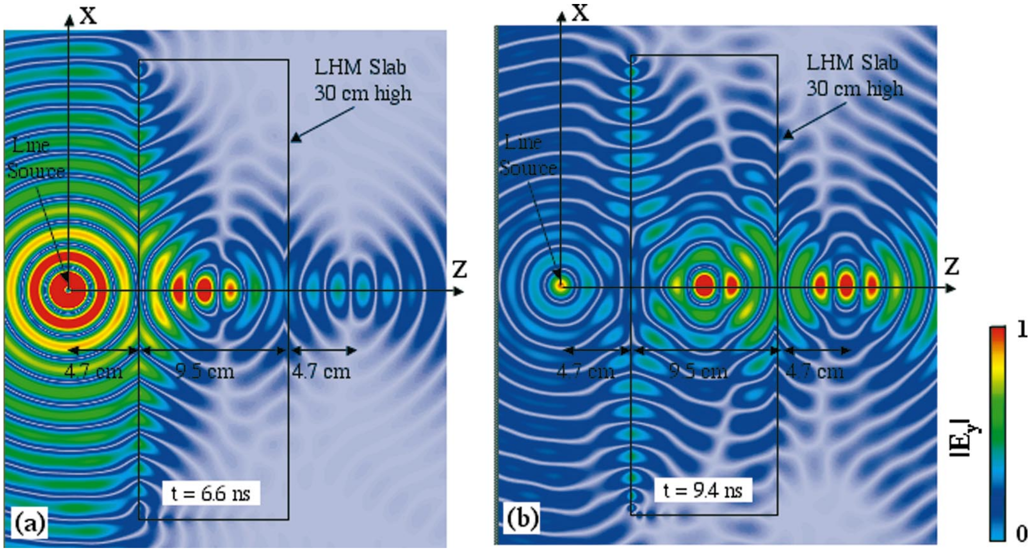

FIG. 11. (Color) Snapshots of the electric field amplitude produced by the Gaussian modulated sine wave illumination of Eq. (2), on a slab with index $n\approx-1.0$ (a) Snapshot taken at $t=6.6$ ns, just as the Gaussian pulse excitation nears its peak; and (b) snapshot at $t=9.4$ ns, well after the pulse has passed. Distinct focal areas are evident, and it can be observed that the focal sizes are consistent with limitations imposed by wave optics.

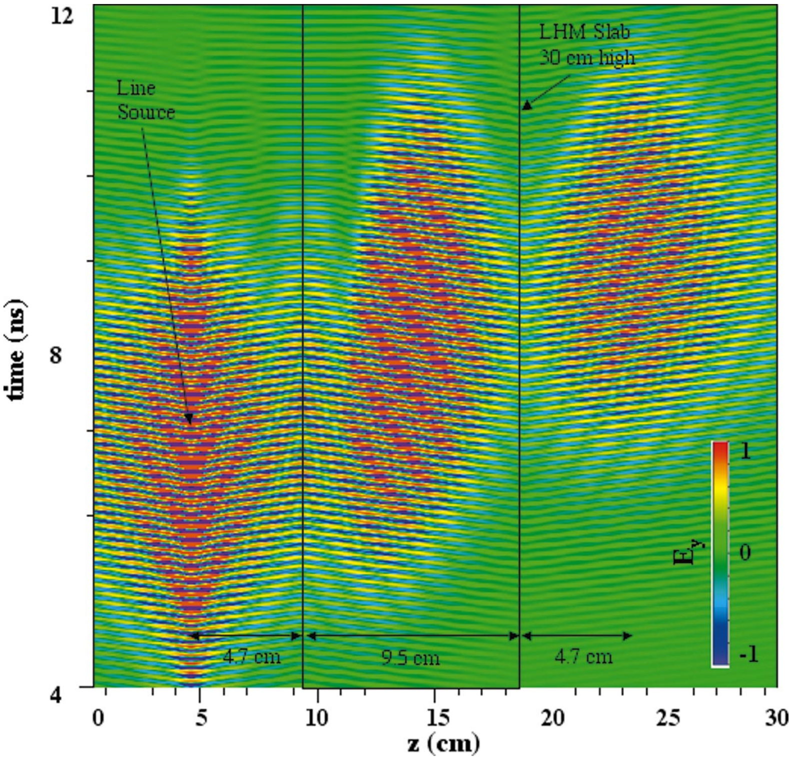

FIG. 12. (Color) Time evolution of E_y in the centerline $(x=0)$, under Gaussian pulse illumination. The figure illustrates how the wave packet comes to a focus in the center of the LHM slab, and is later refocused in the free-space region to the right of the slab (at $t\approx 9$ ns). Although dispersion and loss reshape the wave front and reduce the amplitude, the wave packet maintains its overall shape. The figure is clear indication that negative refraction of the finite duration pulse has occurred. The lack of a "perfect" focus is consistent with limitations imposed by conventional wave optics.

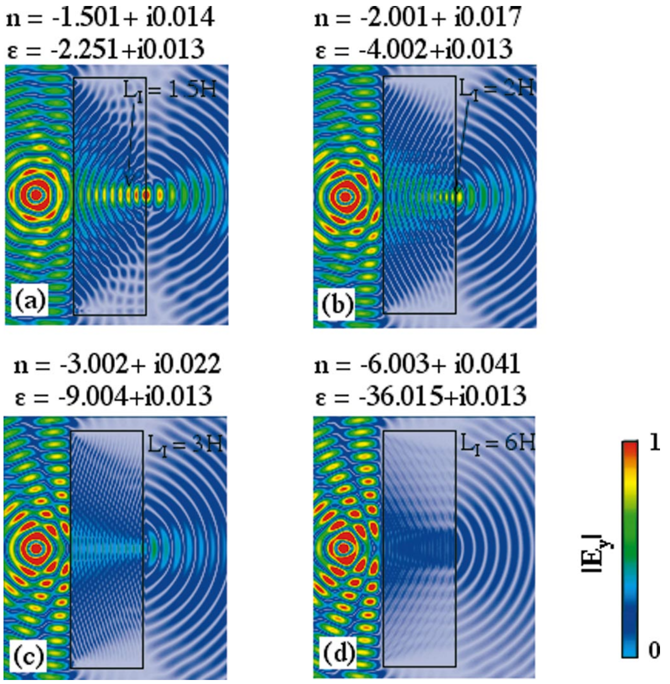
n = -1.501+ i0.014
ε = -2.251+i0.013

n = -2.001+ i0.017
ε = -4.002+i0.013

n = -3.002+ i0.022
ε = -9.004+i0.013

n = -6.003+ i0.041
ε = -36.015+i0.013

FIG. 13. (Color) FDTD snapshots for a LHM slab as the index n is varied from (a) −1.5 to (e) −6.0. The index is varied by changing ε while keeping μ fixed at $-1.001+i0.013$. The images become less well defined due to spherical aberration. When the distance of the first image inside the slab, L_{I} is greater than the slab thickness of $2H$, there are no focused images. Channeling occurs as $n\ll -1$. Prominent interference patterns in front of the slab are due to the large impedance mismatch.

Garcia *et al.*'s claims [10] that the transmission spectral peaks observed by other researchers have been erroneously identified as evidence of LHM behavior and that they are instead evidence of a "zero permeability material." We are also interested in this area because ferrite materials can have a permeability which can assume negative values over a given frequency band. Historical reports indicate that ferromagnetic materials have been observed to exhibit a "ferromagnetic antiresonance" [22] in the vicinity of $\mu\approx 0$. At this resonance, the skin depth becomes very large.

In the following simulations, $\mu(f)$ is chosen to have the same functional form as in Sec. II A 1. For simplicity we set $\mathrm{Re}(\varepsilon)=1$, independent of the frequency. The slab size and source location are the same as those of Sec. II A 1.

The real part of the permeability crosses zero at 12.6 GHz, where we find $\mu=0.000+i0.004$ and $n=0.045+i0.045$. The transmission spectrum for a normally incident plane wave, shown in Fig. 14, indicates there is no peak at $\mu\approx 0$ for $\varepsilon=1.0+i0.0$. Instead, the transmission increases monotonically with frequency until the permeability crosses zero, followed by Fresnel resonances in the region of positive permeability. However, adding an imaginary 0.5 to the permittivity $(\varepsilon=1.0+i0.5)$ results in a transmission peak at the location where the permeability crosses zero (12.6 GHz), much like that observed by Garcia *et al.* [10].

The transmission peak can be understood either from skin depth considerations, as was done in the historical report by Lubitz and Vittoria [22], or from an examination of the complex refractive index. We choose the latter approach. The permittivity and permeability curves are plotted in Figs. 15(a) and 15(b). As an aside, one may notice the small frequency variation to the curve which represents $\mathrm{Im}(\varepsilon)\approx 0.5$. This is because ε is derived from a conductivity model to

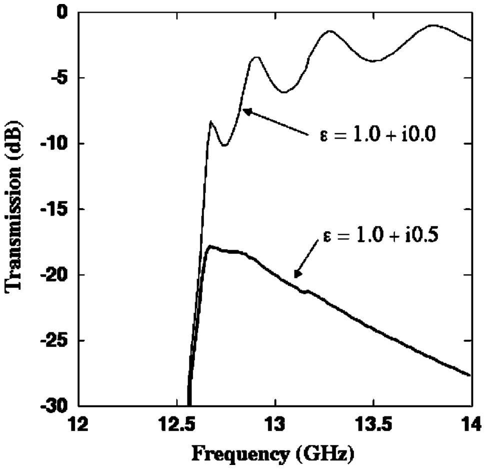

FIG. 14. Transmission of a normal incidence plane wave through a slab having a thickness of 9.5 cm, in the vicinity of $\mu\approx 0$. The upper curve is for a material with $\varepsilon=1.0+i0.0$. The lower curve is for a material with $\varepsilon=1.0+i0.5$. Note the peak in transmission ("ferromagnetic antiresonance") for the lower curve having nonzero $\mathrm{Im}(\varepsilon)$.

ensure causality. The real part of the permeability is seen to cross zero at 12.6 GHz. In Fig. 15(c) the real and imaginary components of the refractive index are plotted for both $\varepsilon=1.0+i0.0$ and $\varepsilon=1.0+i0.5$. Notice the dip in $\mathrm{Im}(n)$, which occurs for $\varepsilon=1.0+i0.5$ but not for $\varepsilon=1.0+i0.0$. It appears that a loss term in the permittivity is necessary for the transmission peak to occur near $\mathrm{Re}(\mu)=0$. More generally, we can see this is true from the definition of n, which can be approximated as $n=\pm\sqrt{\varepsilon\mu}\approx\pm\sqrt{\mathrm{Re}(\varepsilon)\mathrm{Re}(\mu)+i\,\mathrm{Im}(\varepsilon)\mathrm{Re}(\mu)}$ for $\mathrm{Im}(\mu)\approx 0$. The dip in $\mathrm{Im}(n)$ requires $\mathrm{Im}(\varepsilon)>0$.

A snapshot of the fields at 12.6 GHz is presented in Figs. 16(a) and 16(b) which correspond to $\varepsilon=1.0+i0.0$ and $\varepsilon=1.0+i0.5$, respectively. The snapshots show nearly the same amplitude in both instances, very little field penetration beyond the front surface, and very low transmission past the backside boundary. The low amplitude is due to the small intrinsic impedance. Nearly planar wave fronts emerge from the slab as a consequence of the small index. The refractive nature of the $n\approx 0$ slab is clearly distinguishable from that of the $n<0$ slabs which was presented in Figs. 2 and 6. Hence, a planar slab geometry has definite advantages over a wedge for the purpose of measuring the $n\approx 0$ and the $n<0$ regions. It is known [10,11] that measurements using wedges have physical limitations that may lead one to erroneously conclude that a material has a negative index. The finite size leads to diffraction from the tip. Further, material losses cause energy to be transmitted preferentially in the thinner portion of the wedge, causing the radiated the far field to deflect in an ordinary wedge as if the material was left handed.

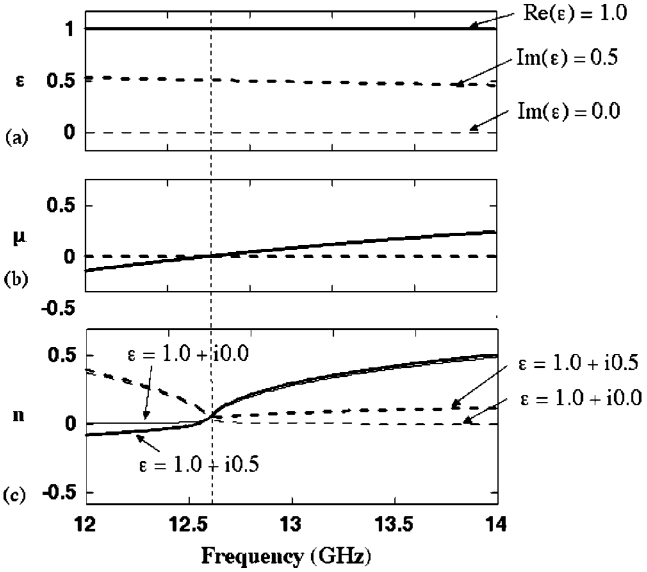

FIG. 15. Constitutive parameters ε, μ, and n, as a function of frequency used to compute the transmission curves in Fig. 14. Notice the dip in $\mathrm{Im}(n)$ in the vicinity of 12.6 GHz, where $\mathrm{Re}(\mu)$ crosses zero, for $\varepsilon=1.0+i0.5$. This dip is the cause of the transmission peak seen in Fig. 14.

3. A material having realistic μ and ε

A known physically realizable material is the SRR structure reported by Smith *et al.* [7]. By analyzing this material we will be in a position to address Smith *et al.*'s claim that such a structure exhibits negative refraction; a line of reasoning disputed by Garcia *et al.* [10].

Along with a description of the SRR geometry, Smith *et al.* provided the frequency dependent permeability. Although the band of frequencies specified is narrow, and only real parts are given, we have fitted the permeability data to a Lorentzian shape to ensure that the material properties are causal and to obtain an estimate of the imaginary part. The permittivity was estimated from Pendry *et al.*'s equation for a wire array [16], which has a Drude frequency dependence. The resulting material parameters and index are plotted in Figs. 17(a) and 17(b), respectively. The transmission coefficient (dB) for a normally incident plane wave on a 4.0 cm thick planar slab of this material is presented in Fig. 17(c). The thickness of the slab was chosen to be $2H=4.0$ cm, large enough to allow the homogeneous model to apply (five SRR periods in the direction of propagation), but not too large to be overwhelmed by the losses. Notice that the real part of the index is negative between 3.5 and 4.0 GHz, and that the transmission peak occurs in this band, at 3.8 GHz (at this frequency $\varepsilon=-5.6+i0.0$ and $\mu=-0.7+i0.1$, resulting in $n=-2.0+i0.2$). We would therefore expect the SRR structure to exhibit negative refraction, the trademark of LHM. The transmission peak does not occur around $\mathrm{Re}(\mu)\approx 0$, as it would for a "zero permeability material," because (as showed in the previous section) a peak in the vicinity of $\mu\approx 0$ is expected only for nonzero $\mathrm{Im}(\varepsilon)$, and here $\mathrm{Im}(\varepsilon)=0.002$ is very small.

To settle this issue we have analyzed the refraction characteristics of a slab made out of this SRR approximate analytical model. We employed a line source located at a distance H in front of the slab and operating at 3.8 GHz, the point of the transmission peak characterized by an index of $n\approx -2$. A snapshot of the field magnitude is shown in Fig. 17(d) and reveals the negative refractive properties exhibited by the SRR structure. Wave fronts inside the slab are seen to

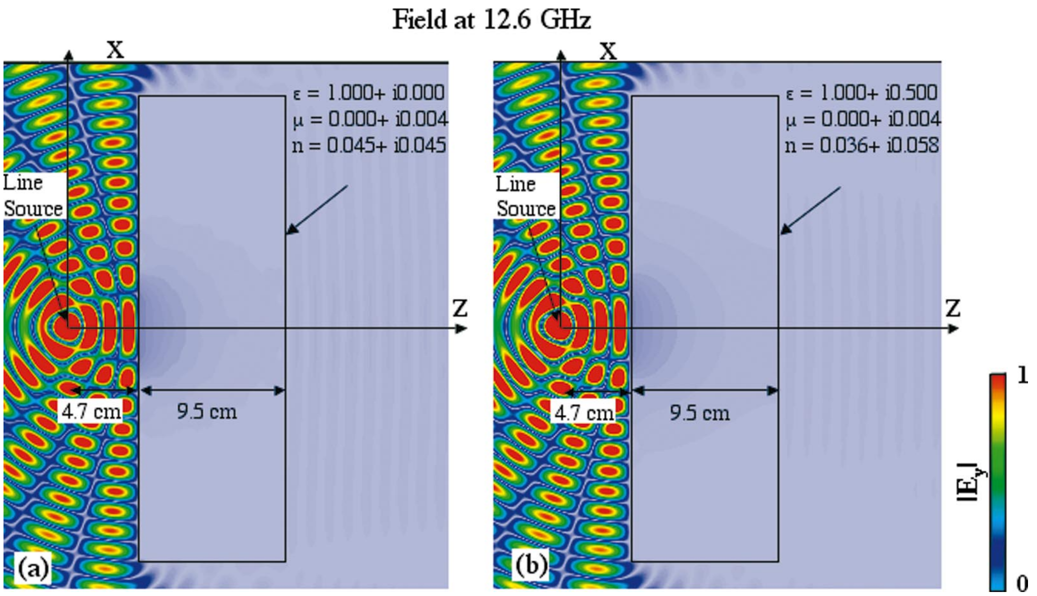

FIG. 16. (Color) FDTD snapshot depicting field distribution under zero permeability conditions at 12.6 GHz. The snapshot is taken at 21 ns and illustrates the reflective properties of the magnetic material slab. The field patterns for (a) $\varepsilon=1.0+i0.0$ and (b) $\varepsilon=1.0+i0.5$ are very similar. The causal permeability is that of Fig. 1.

converge to a spot on the back surface. Nearly circular waves emerge behind the slab from the focal spot, consistent with a material having $\mathrm{Re}(n)=-2.0$. The focal spot is blurred, as it is in Fig. 6(b), due to the spherical aberration effect that occurs for $n\neq-1$. The amplitude of the emerging field is much smaller than the incident field because the intrinsic impedance of the slab is only 35% of the free-space value. We acknowledge this analysis has limitations: (a) the actual SRR structure is anisotropic while the calculations illustrated in Fig 17 were for an isotropic material, and (b) the μ and ε we used were Lorentz and Drude model fits based on the information provided in the report [7]. However, this analysis does clearly provide evidence which support claims that the SRR structure presented in [7] is a LHM in the region of the transmission peak.

III. CONCLUSIONS

We have demonstrated through numerical simulations that frequency dependent causal Lorentzian materials exhibit some interesting optical characteristics, namely, (a) negative refraction when operated in the LHM regime for both cw and

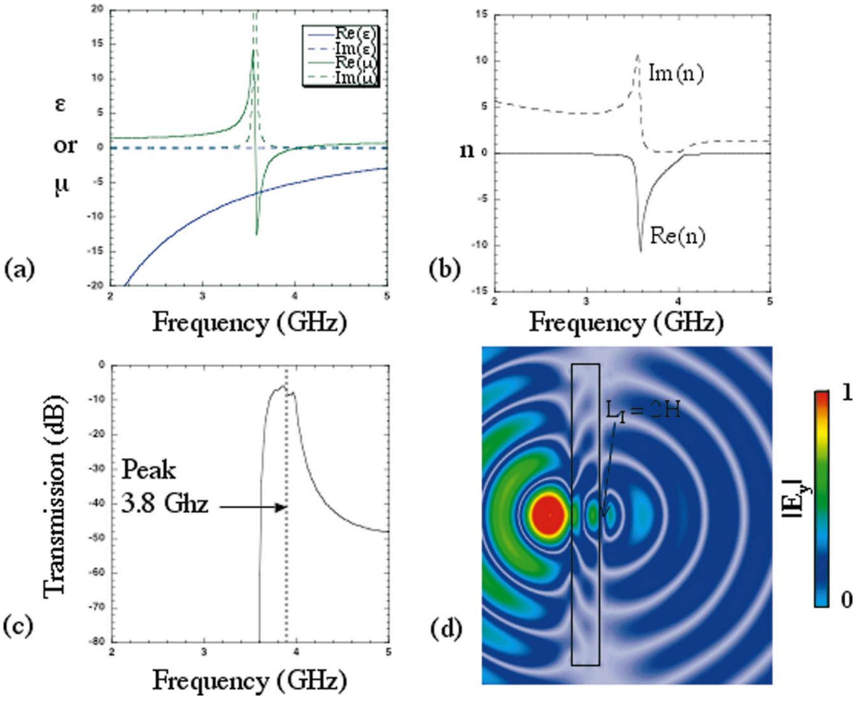

FIG. 17. (Color) Simulated SRR characteristics. (a) Constitutive parameters for the SRR structure described by Smith *et al.* [7]; (b) index of refraction (the real part of the index is negative between 3.5 and 4.0 GHz); (c) transmission coefficient (dB) for a 4.0 cm thick slab showing a peak at 3.8 GHz; (d) snapshot of the electric field magnitude showing focusing on the back of the slab at the peak transmission frequency of 3.84 GHz.

pulsed waves, (b) critical angle phenomena for indices in the range $0 < n < 1$, and (c) a plane wave (spatial) filter effect in the $n \approx 0$ region.

We have exposed the optical phenomena for both impedance matched and more realistic impedance unmatched materials. A "ferromagnetic antiresonance" [22] peak is observed in the vicinity of $\mu \approx 0$ [and a nonzero $\mathrm{Im}(\varepsilon)$], corresponding to Garcia *et al.*'s "zero permeability material" [10], for an unmatched material with a complex permittivity. This type of material acts like both a plane wave filter and a frequency filter. We performed an analysis of Smith *et al.*'s SRR structure [7], and the results do support Smith *et al.*'s claim that the SRR structure is a LHM rather than a "zero permeability material."

ACKNOWLEDGMENT

This work was supported by the DARPA Metamaterials Program.

---

[1] V. G. Veselago, Sov. Phys. Usp. **10**, 509 (1968).
[2] P. M. Valanju, R. M. Walser, and A. P. Valanju, Phys. Rev. Lett. **88**, 187401 (2002).
[3] J. B. Pendry, Phys. Rev. Lett. **85**, 3966 (2000).
[4] J. B. Pendry and S. A. Ramakrishna, J. Phys.: Condens. Matter **14**, 8463 (2002).
[5] D. R. Smith and N. Kroll, Phys. Rev. Lett. **85**, 2933 (2000).
[6] D. R. Smith, W. J. Padilla, D. C. Vier, S. C. Nemat-Nasser, and S. Schultz, Phys. Rev. Lett. **84**, 4184 (2000).
[7] D. R. Smith, D. C. Vier, N. Kroll, and S. Schultz, Appl. Phys. Lett. **77**, 2246 (2000).
[8] R. A. Shelby, D. R. Smith, S. C. Nemat-Nasser, and S. Schultz, Appl. Phys. Lett. **78**, 489 (2001).
[9] R. A. Shelby, D. R. Smith, and S. Schultz, Science **292**, 77 (2001).
[10] N. Garcia, M. Muñoz, E. V. Ponizovskaya, and M. Nieto-Vesperinas, e-print cond-mat/0206476.
[11] M. Sanz, A. C. Papageorgopoulos, W. F. Egelhoff, Jr., M. Nieto-Vesperinas, and N. Garcia, Phys. Rev. E **67**, 067601 (2003).
[12] David R. Smith, David Schurig, Marshall Rosenbluth, and Sheldon Schultz, Appl. Phys. Lett. **82**, 1506 (2003).
[13] F. J. Rachford, D. L. Smith, P. F. Loschialpo, and D. W. Forester, Phys. Rev. E **66**, 036613 (2002).
[14] F. J. Rachford, D. L. Smith, P. F. Loschialpo, and D. W. Forester (unpublished).
[15] J. B. Pendry, A. J. Holden, D. J. Robbins, and W. J. Stewart, IEEE Trans. Microwave Theory Tech. **47**, 2075 (1999).
[16] J. B. Pendry, A. J. Holden, W. J. Stewart, and I. Youngs, Phys. Rev. Lett. **76**, 4773 (1996).
[17] R. W. Ziolkowski and E. Heyman, Phys. Rev. E **64**, 056625 (2001).
[18] N. Garcia and M. Nieto-Vesperinas, Phys. Rev. Lett. **88**, 207403 (2002).
[19] P. F. Loschialpo, D. L. Smith, D. W. Forester, F. J. Rachford, and J. Schelleng, Phys. Rev. E **67**, 026502(R) (2003).
[20] Richard W. Ziolkowski, Opt. Express **11**, 662 (2003).
[21] T. Koschny, P. Markos, D. R. Smith, and C. M. Soukoulis, Phys. Rev. E **68**, 065602(R) (2003).
[22] P. Lubitz and C. Vittoria, in *Magnetism and Magnetic Materials—1973*, edited by C. D. Graham, Jr. and J. J. Rhyne, AIP Conf. Proc. No. 18 (AIP, New York, 1974), p. 507.
[23] The Finite Difference Time Domain simulations were performed with MAXTDA. MAXTDA, written at Georgia Institute of Technology (GTRI), was recently modified by GTRI to include causal Lorentzian functional forms for permittivity and permeability.
[24] J. Berenger, J. Comput. Phys. **114**, 185 (1994).
[25] R. Ruppin, Phys. Lett. A **277**, 61 (2000).
[26] Long Chen, Sailing He, and Lingfang Shen, Phys. Rev. Lett. **92**, 107404 (2004).
[27] S. Enoch, G. Tayeb, P. Sabouroux, N. Guérin, and P. Vincent, Phys. Rev. Lett. **89**, 213902 (2002).